Stochastic modeling and direct simulation of the diffusion media for polymer electrolyte fuel cells

Yun Wang [a,*], Sungchan Cho [a], Ralf Thiedmann [b], Volker Schmidt [b], Werner Lehnert [c], Xuhui Feng [a]

[a] *Renewable Energy Resources Lab (RERL) and National Fuel Cell Research Center, Department of Mechanical and Aerospace Engineering, The University of California, Irvine, CA 92697-3975, USA*
[b] *Institute of Stochastics, Ulm University, 89069 Ulm, Germany*
[c] *Forschungszentrum Jülich GmbH, 52425 Jülich, Germany*

ABSTRACT

This paper combines the stochastic-model-based reconstruction of the gas diffusion layer (GDL) of polymer electrolyte fuel cells (PEFCs) and direct simulation to investigate the pore-level transport within GDLs. The carbon-paper-based GDL is modeled as a stack of thin sections with each section described by planar two-dimensional random line tessellations which are further dilated to three dimensions. The reconstruction is based on given GDL data provided by scanning electron microscopy (SEM) images. With the constructed GDL, we further introduce the direct simulation of the coupled transport processes inside the GDL. The simulation considers the gas flow and species transport in the void space, electronic current conduction in the solid, and heat transfer in both phases. Results indicate a remarkable distinction in tortuosities of gas diffusion passage and solid matrix across the GDL with the former ~1.2 and the latter ~13.8. This difference arises from the synthetic microstructure of GDL, i.e. the lateral alignment nature of the thin carbon fiber, allowing the solid-phase transport to occur mostly in lateral direction. Extensive discussion on the tortuosity is also presented. The numerical tool can be applied to investigate the impact of the GDL microstructure on pore-level transport and scrutinize the macroscopic approach vastly adopted in current fuel cell modeling.

1. Introduction

Fuel cells, converting the chemical energy stored in fuels directly and efficiently to electricity via electrochemical activity, have become the focus of new energy development due to their noteworthy features of high efficiency and low emissions [1–3]. Among all types of fuel cells, the polymer electrolyte fuel cells (PEFCs), also called polymer electrolyte membrane (PEM) fuel cells, have captured the public attention for both mobile and portable applications [4,5].

Among the PEFC components, the gas diffusion layer (GDL) plays an important role of electronic connection between the bipolar plate with channel-land structure and the electrode. In addition, the GDL performs the following functions essential to fuel cell operation: passage for reactant transport and heat/water removal, mechanical support to the membrane electrode assembly (MEA), and protection of the catalyst layer from corrosion or erosion caused by flows or other factors [6,7]. Physical processes in GDLs, in addition to diffusion, include bypass flow induced by in-plane pressure difference between neighboring channels [8,9],

through-plane flow due to mass source/sink by electrochemical reactions [10,11], heat transfer [12,13], heat pipe phenomena [14], two-phase flow [14–18], and electron transport [19–21], to list just a few.

The carbon paper is a common GDL material used in PEFCs. It is non-woven carbon-fiber-based porous media, where carbon fibers are randomly placed and bonded by binders. Fig. 1 shows a picture of carbon papers. Modeling the transport inside GDLs is an essential part of a fuel cell model due to the vital role of GDLs. Current effort in modeling is overwhelmingly through the macroscopic description. This approach assumes a homogenous structure of GDL and therefore defines several effective parameters accounting for micro structural features, e.g. porosity and permeability. These parameters are also adopted for modeling other GDL materials, e.g. the carbon cloth and Sigracet GDLs, and set differently according to their structural characteristics.

Transport in the GDL, e.g. water and oxygen diffusion, are closely related to fuel cell voltage loss, e.g. the mass transport and ohmic losses. Typically, diffusion dominates gaseous species transport in GDLs. Convection may be induced by the local mass sink/source due to the reaction activities in the catalyst layer [11]. The convection contributes little comparing with the diffusive one in most cases [11,22]. Some special designs [8,9] are reported,

* Corresponding author. Tel.: +1 949 824 6004; fax: +1 949 824 8585.
E-mail address: yunw@uci.edu (Y. Wang).

Nomenclature

C	molar concentration of species k, mol/m^3
D	species diffusivity, m^2/s
F	Faraday's constant, 96,487 C/equivalent
I	current density, A/cm^2
J	transfer current density, A/cm^3
K	permeability, m^2
P	pressure, Pa
R	universal gas constant, 8.134 J/mol K
T	temperature, K
$\vec{u}$	velocity vector, m/s

Greeks

α	net water flux per proton flux
ρ	density, kg/m^3

Φ	phase potential, V
ε	porosity
$\overset{\Rightarrow}{\tau}$	shear stress, N/m^2
σ	electronic or ionic conductivity, S/m

Superscripts and subscripts

c	cathode
D	diffusion
g	gas phase
GDL	gas diffusion layer
k	species
o	gas channel inlet value; reference value
s	solid

where convection plays an important role. In addition to species transport, the reaction heat is removed via the GDL, primarily by heat conduction in the solid matrix. Recently, liquid water transport within GDLs received much attention. Liquid may block the pore space, hampering reactant supply. Liquid flow in GDLs is primarily driven by the capillary action. Its macroscopic modeling is commonly based on the Darcy's law and the knowledge of the capillary pressure in porous media [18].

Though great efforts have been made to investigate the macroscopic phenomena, few are proposed to study the pore-level transport within the GDL. The macroscopic model requires empirical correlations such as the effective coefficients to account for the porous media property. These correlations can be developed from the pore-level information obtained from direct modeling/simulation. In addition, the pore-level study can provide fundamental details regarding interaction between transport and pore structure, which is beyond the capability of a usual macroscopic model. The direct simulation is a powerful numerical tool for studying the transport in porous media. Some also named it the direct numerical simulation (DNS) [23–25]. To distinguish with the terms in the computational fluid dynamics (CFD), e.g. in the turbulent simulation, we follow Kaviany [26,27] and choose the term of direct simulation for this numerical technique. The direct simulation requires precisely capturing the GDL morphology. Several techniques have been applied to acquire synthetic microstructures of GDLs [28–32]. An important aspect of a suitable GDL-reconstruction model is the possibility of fitting it to real data. This paper employs the stochastic model of GDLs developed in [28]. The optimal parameters of the fitted fiber model are gained using 2D projection

images from electron microscopy. Therefore in Ref. [28] proper segmentation algorithms are applied to obtain the required structural information from these 2D images. This means that the model is fitted with respect to structural characteristics but not with respect to physical properties. The direct simulation model based on realizations of this stochastic GDL approach is further introduced to study the pore-level phenomena. The fact that the model is fitted to real data using only structural information of real images allows the unbiased computations of physical parameters as will be done in this paper. A typical porosity of $\sim$0.78 of GDLs is considered, which is close to the state of GDLs without compression or the part of the GDL under the channel [32]. We consider a typical fuel cell operating condition and solve the fluid, species, heat and electron equations simultaneously within the GDL. Pore-level information is presented and discussed.

2. Stochastic modeling of GDLs

In this section we give a short description of the stochastic multi-layer model for reconstructing the GDL microstructure that is based on tools from stochastic geometry [34,35]. For details regarding this model and its implementation we refer to Ref. [28].

2.1. Modeling of the fiber system

A look at Fig. 1 leads to an impression that the carbon fibers of Toray paper can be approximated by horizontally orientated straight lines (assume negligible curvature) which are dilated with respect to 3D. This can also be verified through the production
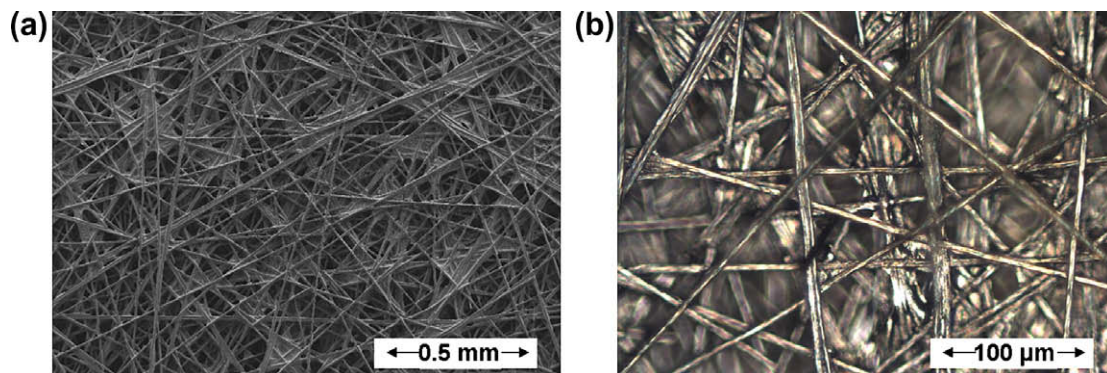

Fig. 1. Microscope images of the carbon paper diffusion media used in PEFCs.

process of the carbon-paper-based GDL, where fibers are disposed "almost" horizontally. In addition, it is assumed that the fiber system can be seen as a stack of several thin sections consisting of such horizontally/laterally orientated fibers which are allowed to interpenetrate. Therefore the fiber system is modeled as a stack of independent and identically distributed layers, where adjacent layers are just touching each other. Note that this assumption is a simplification in comparison to the real GDL because the fibers in one thin section are crossing each other to a small extent, which is neglected in the model. Here, the fibers within a given thin section are seen as mutually penetrating cylinders or filaments. In [28] it was shown that despite of these simplifications the structure of this model and the structure of physically measured 3D data of such GDLs are very similar. In [36], tortuosity describing characteristics, pore size distributions, and connectivity properties of the pore space have been computed for the model and also for real (physically) measured 3D data. The results for the model and the real measured 3D data are also very close together with respect to such transport relevant properties. So this model seems to be appropriate for the here considered kind of GDL.

The model for the fibers in each section is based on Poisson line tessellations (PLT) in the plane. A planar line tessellation is a set of cells $\xi_1, \xi_2, \ldots$ generated by intersecting lines $l_1, l_2, \ldots$ scattered in the plane. A line l_n in the plane can be represented by its normal form, i.e. its orthogonal signed distance to the origin x_n and its direction m_n measured as the angle to the x-axis (see Fig. 2(a)). Thus a line tessellation can be seen as an independently marked point process $(X_1, M_1), (X_2, M_2), \ldots$ where in case of a PLT the random distances $X_1, X_2, \ldots$ form a homogeneous Poisson point process on the real line with intensity $\lambda > 0$. The random variables $M_1, M_2, \ldots$, describing the directions, are uniformly distributed in the interval $[0, \pi)$ and mutually independent as well as independent from the Poisson point process. The PLT is then the set of random polygons $\Xi_1, \Xi_2, \ldots$ created by the random lines $(X_1, M_1), (X_2, M_2), \ldots$ (see Fig. 2(b)). The PLT is completely described by one parameter, the intensity of the Poisson point process $\lambda > 0$, which can be interpreted as the mean total edge length per unit area of the PLT.

The lines of the PLT are one-dimensional objects. To get a 3D model for the fibers the lines are dilated with respect to 3D [35]. Mathematically this can be described by the Minkowski sum which is defined for two sets $A \subset R^3$ and $B \subset R^3$ by

$$A \oplus B = \{a + b : \ a \in A, \ b \in B\} \tag{1}$$

To model a complete layer of the multi-layer model, the set of all edges $\bigcup \partial \Xi_i$ is dilated by a structuring element C_r, e.g. a ball with radius r or a cube with side length $2r$, centered at the origin. The cube seems in some cases to be the most realistic approximation because of the resolution of the discretized model. This was shown in Ref. [28], where the spherical contact distribution (see Ref. [35]) was applied. In the following a fiber diameter of 7.5 μm and a voxel resolution of 1.5 μm will be considered, following the real 3D GDL data in [28]. This implies that the fiber diameters have to be modeled by 5 voxels.

The complete multi-layer model consists then of a stack of such dilated PLTs (see Fig. 3), where all layers are assumed to be independent and identically distributed. Adjacent layers are just touching each other.

2.2. Modeling of the binder

The fibers of the GDL are adhered by means of a binder, which is introduced in the manufacturing process and can be treated as thin films bounded by fibers. The binder is modeled by an independent filling of cells, i.e. a cell of the underlying PLT is chosen to contain binder with probability $p \in [0, 1]$ (see Fig. 4).

2.2.1. Structural fitting of the multi-layer model to real data

The considered model for fibers and binder leads to the following formulae for the volume fractions as described in Refs. [28] and [36], respectively. For notation we use $2r$ for describing the side length of the cube which is used to dilate the lines of the PLT, γ denotes the intensity of the PLT in each layer, and p denotes the probability that a cell is filled with binder. The expected volume fraction of fibers $V_{fiber}(\gamma, r)$ is then given by
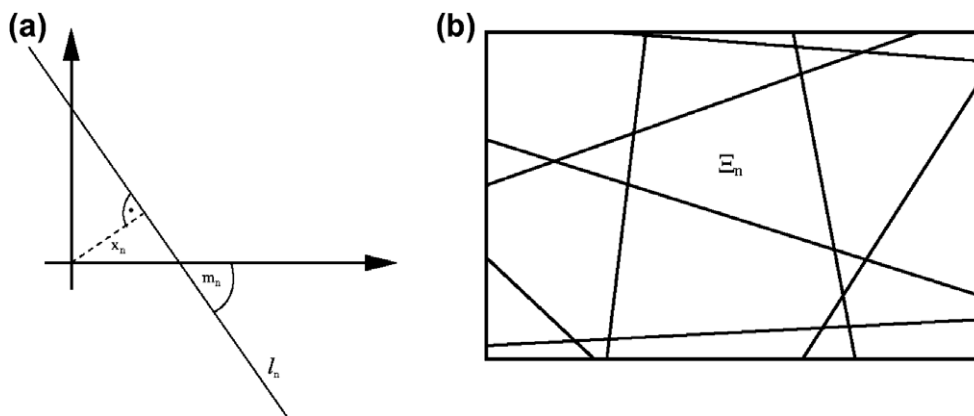

Fig. 2. (a) Construction of a line and (b) a cell Ξ_n of a PLT.

Fig. 3. Schematic display of the multi-layer model: (a) one layer, (b) two layers, and (c) several layers.
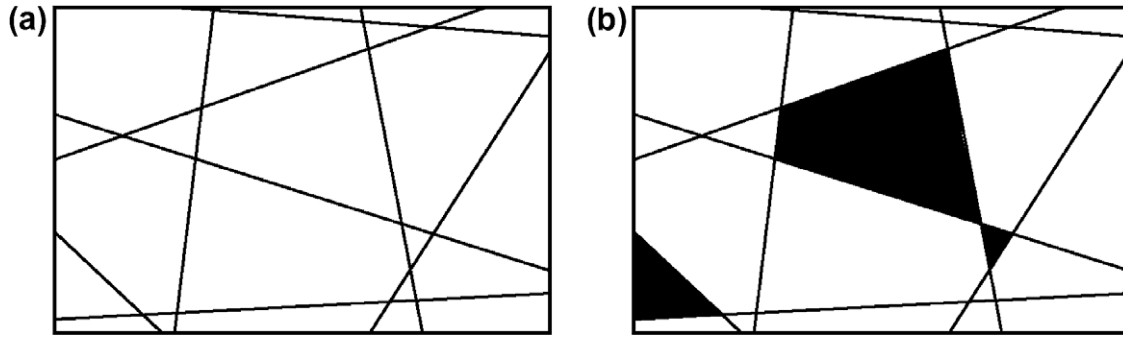
(a) **(b)**

Fig. 4. (a) Cells without binder and (b) some cells filled with binder.

$$V_{fiber}(\gamma, r) = 1 - \exp(-2r\gamma) \tag{2}$$

The expected volume fraction of binder $V_{binder}(\gamma, r, p)$ is given by

$$V_{binder}(\gamma, r, p) = p \exp(-2r\gamma) \tag{3}$$

Additionally, the relationship $\varepsilon = 1 - (V_{fiber}(\gamma, r) + V_{binder}(\gamma, r, p))$ holds, where ε denotes the (mean) porosity of the considered GDL. In [28], the value γ was estimated from 2D SEM images for the here considered material where a non-interactive segmentation algorithm for the detection of the top section has been applied. From the segmented data the intensity of the PLT was then estimated by 0.025. From 3D images of the same kind of material, gained by means of synchrotron tomography, in [28] the (mean) porosity ε was estimated 78%. This value of ε for Toray 090 GDL structures is also known from the literature [33]. If these values are plugged in the above given relationship, the estimated value for p is 0.059 which corresponds to a volume fraction of binder of 4.9% in the 3D GDL structure. A realization of the complete model can be seen in Fig. 5. A validation of the model with its fitted parameters was done in [28] by the spherical contact distribution function, see [35]. This characteristic describes the minimum distance of an arbitrarily chosen point of the pore space to the fiber or binder system, respectively. Additionally, in [36] it is reported that the model and real measured 3D data are also very similar with respect to tortuosity describing characteristics, pore size distribution, and connectivity properties of the pore space.

3. Direct simulation

3.1. Mathematical modeling

In this section, a small representative GDL is considered for numerical simulation (see Fig. 5). One side surface of the GDL normal to x direction attaches the catalyst layer or MPL (microscopic layer), while the other in connection to the channel/land region. The physical transports within GDLs are linked to the electrochemical activities in the catalyst layer, where the following electrochemical reaction takes place

$$O_2 + 4e^- + 4H^+ \rightarrow 2H_2O + heat \tag{4}$$
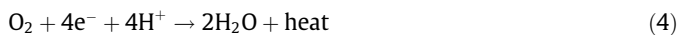
The reaction consumes oxygen, protons, and electrons, and produces both heat and water. Among these species, the electron and oxygen supplies rely on the GDL, while heat and water are removed via both GDL and the electrolyte membrane. In addition, the electronic current is conducted through the solid matrix of carbon fibers, oxygen and water transport in the void, while heat transfer occurs in both phases. When excess water is present, liquid water will emerge, flooding the electrode and GDL. Two-phase (liquid–gas) transport in fuel cell GDL is a complex phenomenon. It has been widely investigated in fuel cell literature, mostly in the macro-scopic view, and the research is still on-going. In this paper, our focus is placed on introduction of the combination of the stochastic modeling and direct simulation; therefore we exclude the liquid transport in the work. The results can benefit the study of the low-humidity operation and transport characteristics of the carbon paper GDL.

3.1.1. Void space

The void space in the GDL is mostly interconnected and allows gas flow. In the direct simulation of GDL, a fine mesh is applied that is able to distinguish the void and solid. In the void space, the Navier–Stokes equation can be applied to describe the fluid motion

$$\frac{\partial \rho^{(g)}}{\partial t} + \nabla \cdot \left(\rho^{(g)} \vec{u}^{(g)} \right) = 0 \tag{5}$$

$$\left[\frac{\partial \rho^{(g)} \vec{u}^{(g)}}{\partial t} + \nabla \cdot \left(\rho^{(g)} \vec{u}^{(g)} \vec{u}^{(g)} \right) \right] = -\nabla P^{(g)} + \nabla \cdot \vec{\vec{\tau}} \tag{6}$$

Note that the quantities in the above are defined at the pore level, therefore macroscopic characteristics of porosity and permeability no longer appear in the equation.

The void pores also provide passages for species transport. In addition to the convection induced by the mass flow, diffusion is a major mechanism for water and oxygen transport. At the pore level of the GDL, the molecular diffusion still dominates and the transport equations can be unified as

$$\frac{\partial C^k}{\partial t} + \nabla \cdot (\vec{u}^{(g)} C^k) = \nabla \cdot (D^k \nabla C^k) \tag{7}$$

where the superscript k denotes species and the diffusion coefficient D^k depends on the local condition

$$D^k = D_0^k \left(\frac{T}{353} \right)^{3/2} \left(\frac{1}{P} \right) \tag{8}$$

Note that different to the macroscopic model no modifications of the diffusion coefficient are needed in the direct simulation description. The characteristics of the GDL structure are already contained in the fine mesh of the direct simulation.

In addition, in the gaseous phase heat transfer occurs and the energy equation reads

$$\rho^{(g)} c_p^{(g)} \frac{\partial T^{(g)}}{\partial t} + \nabla \cdot \left(\rho^{(g)} c_p^{(g)} \vec{u}^{(g)} T^{(g)} \right) = \nabla \cdot (k^{(g)} \nabla T^{(g)}) \tag{9}$$

3.1.2. Solid phase

The solid matrix consists of the carbon fibers and binder. The solid matrix is the media for the electron transport, which can be described by

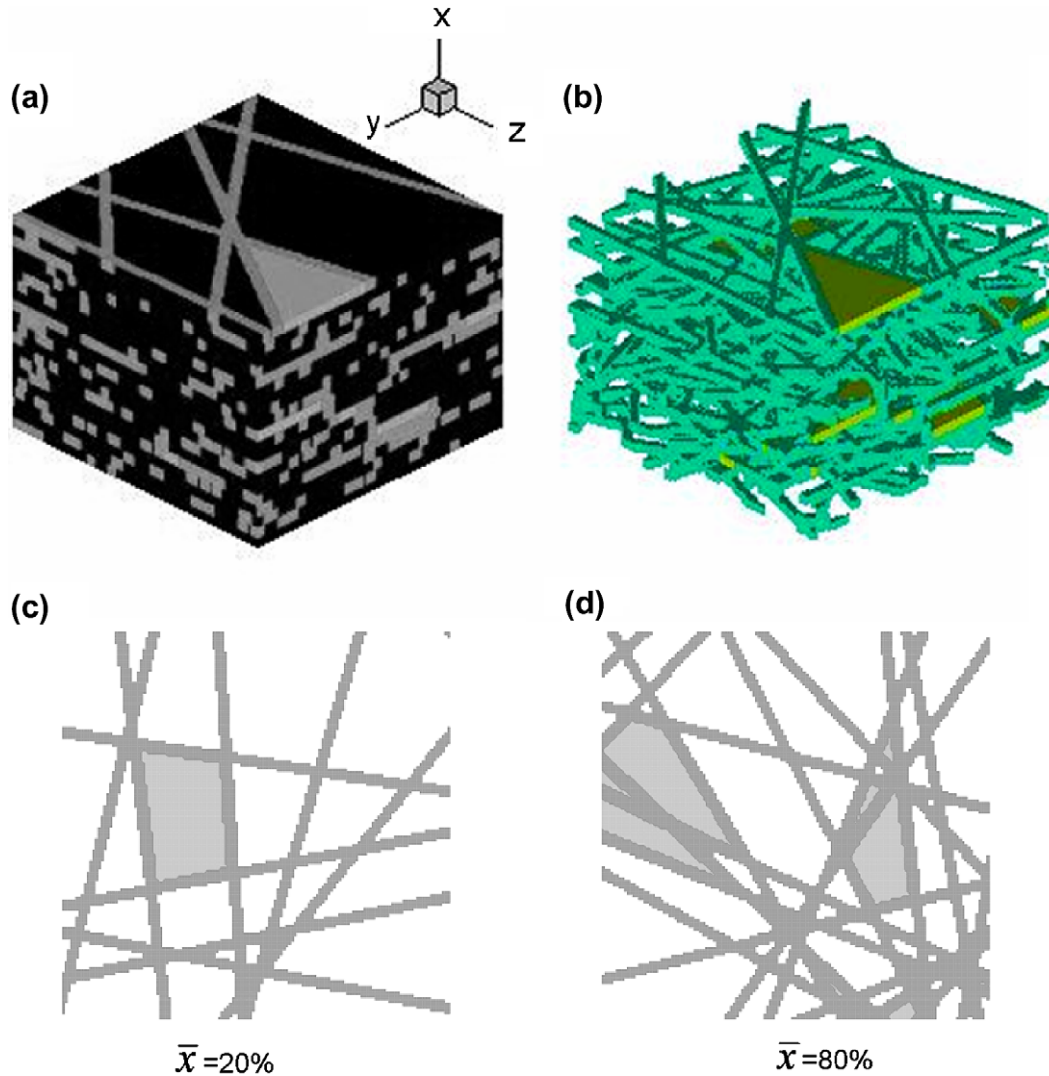$$0 = \nabla \cdot (\sigma_s \nabla \Phi^{(s)}) \tag{10}$$

Fig. 5. (a) A realization of the stochastic model for carbon paper GDL reconstruction; (b) the solid matrix; (c) solid matrix cross-section at $\bar{x} = 20\%$; and (d) solid matrix cross-section at $\bar{x} = 80\%$.

The above equation is applied to both carbon fibers and binders by setting proper values of model parameters according to the material properties. In practice the binder material may vary. We assume identical properties of these two solids in this study.

In both phases, energy equation is applied and can be unified as

$$\frac{\rho^{(s)}c_p^{(s)}\partial T^{(s)}}{\partial t} = \nabla \cdot (k^{(s)}\nabla T^{(s)}) + \frac{\vec{i}_e^2}{\sigma_s} \tag{11}$$

with the electronic current flux

$$\vec{i}_e = -\sigma_s \nabla \Phi^{(s)} \tag{12}$$

3.2. Boundary conditions

Though a 3D GDL is considered, we focus on phenomena in the through-plane (x) direction, i.e. from the catalyst layer to the channel. The lateral transport will occur due to the 3D structure of the GDL. In addition, to simplify setting boundary conditions, a highly conductive artificial layer is added to the left side of the GDL where each computational grid contains both solid and gas, and thus allows solid- and gas-phase transport in each grid, i.e. the conservation equations apply in the region of this layer without

distinguishing the solid and gas phases. Note that due to the conservation principle applied, the fluxes set on the surface of this pseudo layer, such as heat and electron, will equal to the ones into/out of the GDL.

3.2.1. GDL surface near the catalyst layer

In the catalyst layer, water and heat are produced while oxygen and electrons are consumed. At the boundary or the interface between the GDL and catalyst layer, fluxes of oxygen, water, heat and electrons will be induced. The magnitude of the flux is determined by the reaction rate and transport to the anode side.

Water is added to the cathode by water production and electro-osmatic drag. Both are proportional to the current density. Part of water will return back to the anode through back-diffusion. Quantifying the amount of water back diffused requires information of water level in the anode. In absence of anode water content, the net water transfer coefficient, α, is frequently used to combine the effects of water back-diffusion and electro-osmatic drag. Its value is around 0, typically positive. The water flux at this boundary can then be written as

$$\left(-D^{H_2O}\frac{\partial C^{H_2O}}{\partial x} - \vec{u} \cdot \vec{n}C^{H_2O}\right) = (1+2\alpha)\frac{I}{2F} \tag{13}$$

where F is the Faraday constant and I current density. In fuel cell operation, I may vary spatially according to local operating condition.

Oxygen is consumed in the cathode. In real case, a small amount of oxygen may cross the membrane reaching the anode. Neglecting the oxygen cross-over, its flux at the boundary can be expressed according to its consumption rate

$$\left(-D^{O_2} \frac{\partial C^{O_2}}{\partial x} - \vec{u} \cdot \vec{n} C^{O_2} \right) = -\frac{I}{4F} \tag{14}$$

In the cathode, electrons are consumed in the electrochemical reaction in Eq. (4). The electrolyte membrane typically has an extremely low electronic conductivity, therefore most studies only consider electrons from the GDL side. Following the same assumption, the electronic current at the boundary can then be written as

$$-\sigma_s \frac{\partial \Phi^{(s)}}{\partial x} = I \tag{15}$$

Mass flows will be induced in the cathode due to the reaction activities. Ref. [11] identifies three major mechanisms that may contribute the mass source/sink in the gas phase. Based on their evaluation, electro-osmatic drag and back-diffusion may play an important role in the induced mass flow. This mass source/sink occurs in the catalyst layer, which, expressed as rate per volume, can be derived as

$$S_m = M^{H_2O} \nabla \cdot (D_m^{H_2O,eff} \nabla C^{H_2O}) + M^{O_2} \frac{j}{4F} - M^{H_2O} \frac{j}{2F} - M^{H_2O} \nabla$$
$$\cdot \left(\frac{n_d}{F} \vec{i}_p \right) \tag{16}$$

where j is the transfer current density and $\vec{i}_p$ the protonic current flux. j also varies from place to place including across the catalyst layer [37]. An integral can be taken for the above equation across the catalyst layer to obtain the surface flux. Again by adopting the net water transfer coefficient α, the mass flux can be set

$$-\rho \vec{u} \cdot \vec{n} = \left(\frac{I}{2F} M^{H_2} + \alpha \frac{I}{F} M^{H_2O} \right) \tag{17}$$

The produced heat is taken away from the electrode via the GDL. Most of heat is generated in the cathode due to the irreversible process. Other heating mechanisms such as Joule heat arising from the ionic resistance and anode reaction heat also occur in the MEA. The heat in the MEA is removed via both anode and cathode GDLs. Assuming half of the heat enters the cathode GDL, the boundary condition for energy equation can be written as

$$-k \frac{\partial T}{\partial x} - \vec{u} \cdot \vec{n} \rho C_p T = \frac{1}{2} (Eo - V_{cell}) I \tag{18}$$

where E_o is defined as $-\frac{\Delta h}{2F}$ and represents the EMF (electromotive force) that all the energy from hydrogen/oxygen, the 'calorific value', heating value, or enthalpy of formation, were transformed into electrical energy with water vapor as the reaction product.

3.2.2. GDL surface near the gas channel

On the right side, GDL connects to the gas channel. In the channel, a stoichiometry around 1.5–2 is typically used in practice. The air flow is also partially or fully hydrated prior to injection. The channel velocity is typically ~1 m/s, therefore channel stream is featured as a low Re laminar flow. The gradients of quantities such as oxygen and water contents along the channel are small comparing with the in- or through-plane ones, therefore, we assume constant values at the outer surface of the small part of GDL considered. The conditions at this boundary are

$$\frac{\partial}{\partial n} \begin{pmatrix} \vec{u} \\ P \end{pmatrix} = 0 \quad \text{and} \quad \begin{pmatrix} C_{O_2} \\ C_w \\ T \\ \Phi^{(s)} \end{pmatrix} = \begin{pmatrix} C_{O_2}^{ch} \\ C_w^{ch} \\ T_{cell} \\ V_{cell} \end{pmatrix} \tag{19}$$

3.2.3. Void-solid interface

Within the computational domain, we apply equations in each grid according to the phase it represents. For the void, flow and species equations are applied. At the surface of the solid matrix, the no-slip and no-flux boundary conditions are set. For electron equation in the solid, no-flux condition is applied at the solid surface. As to energy equation, temperature and heat flux are continuous across the interface.

3.3. Numerical procedures

The construction of the random lines or PLT, respectively, has already been described in Section 2, where also the filling of the cells with binder can be found. For the numerical simulations, the realizations of the stochastic multi-layer model are discretized, where a voxel resolution of 1.5 µm is applied. The governing equations, Eqs. (5)–(11), along with their appropriate boundary conditions, are discretized by the finite volume method, with SIMPLE (semi-implicit pressure linked equation) algorithm [38]. The SIMPLE algorithm is to update the pressure and velocity fields from the solution of the pressure correction equation, solved by algebraic multi-grid (AMG) method. Following the solution of the flow field, energy, species, and electron equations are solved. Detailed numerical discretization can be found in Ref. [18]. About ~2 million (140 × 140 × 100) uniform computational cells are used to describe the complex structure of a GDL (0.21 × 0.21 × 0.15 mm) and internal transport phenomena. Geometrical parameters and physical properties are listed in Table 1. In all the numerical simulations to be presented in the next section, the equation residuals in all are smaller than 10^{-6} and the values of species (e.g. O_2 and H_2O) and energy global imbalances are all less than 0.1%. A typical simulation takes about 5 h with ~2000 iterations based on a single personal computer (CPU 3.0 GHz and 3.5 GB RAM).

4. Results and discussion

The GDL is reconstructed by setting the parameter for the fibers as detected from 2D images and the (mean) porosity as detected from 3D images, see Ref. [28], which is about 78%. This level of porosity fits the portion of the GDL under channels where no compression is imposed on the GDL [33]. The realization of the GDL model is shown in Fig. 5. A standard operating condition, 0.5 V and 1.0 A/cm^2, is considered in the direct simulation to display the microscopic transport occurring in the GDL.

Table 1
Geometrical, physical, and operating parameters.

Quantity	Value
Fiber cross-section dimension (side length)	7.5 µm
GDL thickness, δ	0.15 mm
Pressures, P	2.0 atm
Porosity of GDLs, ε	0.78
Thermal conductivity of air, $k^{(g)}$	0.025 W/m K
Thermal conductivity of carbon fibers and binders, $k^{(s)}$	10 W/m K
Electronic conductivity of carbon fibers, σ_s	20,000 S/m
Species diffusivity in cathode gas at standard condition, $D_{o,O_2/w}$	$3.24/3.89 \times 10^{-5}$ m^2/s

Fig. 6 shows the velocity distributions at three typical locations. It can be seen that the local velocity can reach ~0.001 m/s caused by the mass addition in the cathode, mostly velocity is order-of-magnitude smaller, which is consistent with the prediction by the macroscopic models [11,18]. The carbon fibers are 7.5 μm in diameter, therefore the flow can easily go around the fibers. However, the binders are typically flat connecting fibers and have much larger blocking areas than a single fiber, forcing the flow to go horizontally/laterally. Strong flows are indicated near the interstitial space primarily due to blockage of the binders. This figure also indicates that the flow is highly non-uniform due to the stochastic microstructure of the GDL. Despite that local flow may reach 0.003 m/s, the induced convective transport of species is weak comparing with the diffusion as indicated by the local Peclet number

$$Pe = \frac{u \delta_{GDL}}{D_g} < 0.1 \qquad (20)$$

In addition, through the average pressure drop one can obtain the through-plane permeability K of 3.1×10^{-12} m² for this part of porous media using the Darcy's law

$$\vec{u} = -\frac{K}{\mu} \nabla P \qquad (21)$$

This value is consistent with that used in the literature [6,18,39] and is slightly lower than the one calculated from the Carman–Kozeny model primarily due to the role of the binder

$$K = \frac{\varepsilon^3}{180(1-\varepsilon)^2} d^2 \qquad (22)$$

In addition, Fig. 7 displays the flow distributions for two different net water transfer coefficients, $\alpha = 0.5$ and -0.5. At the case of $\alpha = 0.5$, more water mass is added to the cathode, which may happen at the beginning of the cathode channel when dry condition is applied in the cathode while the anode is fed with hydrogen at high humidification. Such an example can be found in Ref. [11]. Due to the increased mass addition, the magnitude of the induced velocity is significantly increased (over 5 times). This is also consis-

tent with the conclusion from Ref. [11], which shows that water activity plays vital role in the mass flow in GDLs. Despite of the flow magnitude, the flow direction varies little. For the other case, i.e. $\alpha = -0.5$, the flow reverses with slightly smaller magnitude in its velocity. The case of a negative α frequently happens for the counter flow near the cathode outlet and anode inlet, where abundance of produced water can diffuse to the anode to humidify the dry hydrogen. As mass is withdrawn in the cathode in this case, the flow will be promoted from the channel to the catalyst layer. As the flow conductance is determined by the structure of solid matrix which is the same as the case of the positive α, the flow distribution is similar to Fig. 7(a) except the direction.

Fig. 8 shows the temperature distributions at the three locations of the GDL. As the thermal conductivity of the solid matrix is several-order-of-magnitude higher than the air, heat conduction mostly takes place via the randomly placed fibers. Therefore, temperature varies in all the directions (x, y, and z directions) as indicated in this figure. In addition, the temperature variation within the local pore $\triangle T_d$ is ~0.2 K. The locations of carbon fibers are indistinguishable from voids in the contours. This can be explained by the small pore dimension and negligible convection in the gas phase. Note that the temperature variation through the GDL, the system level $\triangle T_L$, is only ~1 K, which is comparable to the pore one $\triangle T_d$, raising the concern of local thermal equilibrium [26]. In addition, the $\triangle T_L$ of ~1 K is consistent with our previous prediction and analysis [14,22].

Fig. 9 shows the oxygen concentration contours in the void. A small variation of the oxygen content, ~1 mol/m³, in the through-plane direction is indicated. In addition, a low oxygen concentration appears in the lower-left corner of Fig. 9(a), which can be explained by the local binder blockage (see Fig. 6(a)). Similar contours can be drawn for water vapor concentration except that the gradients reverse. Also from the structure of the diffusion media it is evident that the tortuosity of the pore space is much smaller than that of the solid matrix. This characteristic can be defined as the ratio of the mean effective path length through the pore space of a porous material and the material thickness [40,41]. In the literature, the tortuosity is usually described as a property of porous media, defined as the ratio of the actual path
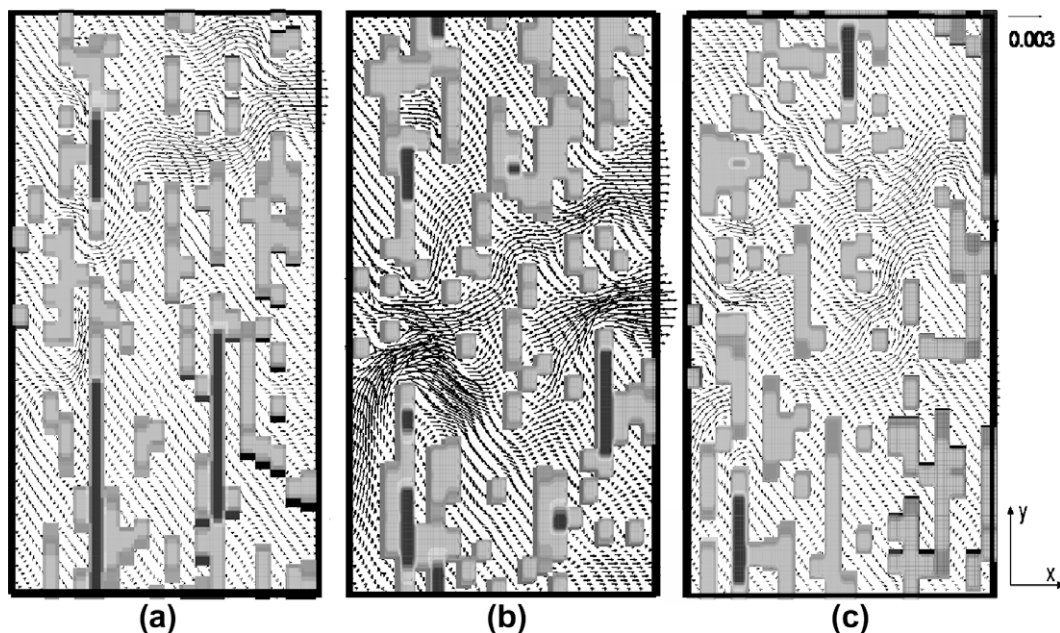

Fig. 6. Flow fields at different portions of the GDL for $\alpha = 0.05$: (a) $\bar{z} = 0.25$; (b) $\bar{z} = 0.5$; and (c) $\bar{z} = 0.75$. $\bar{z}$ is the dimensionless distance in z direction ranging from 0 to 1. The gray region denotes the solid with the light gray being the carbon fibers and the dark the binders.
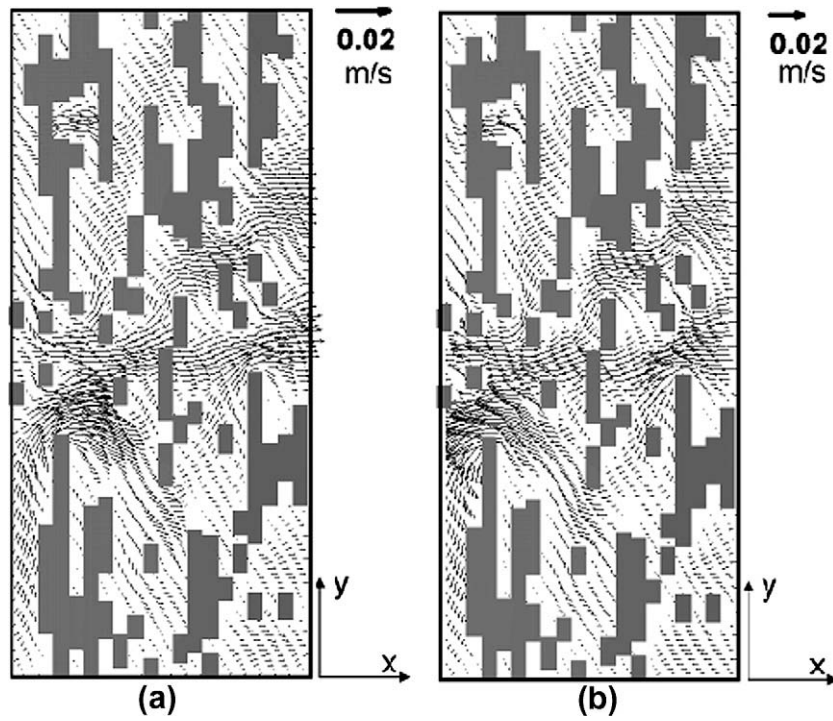
Fig. 7. Flow fields at the portion ($\bar{z} = 0.5$) of the GDL for (a) $\alpha = 0.5$ and (b) $\alpha = -0.5$.
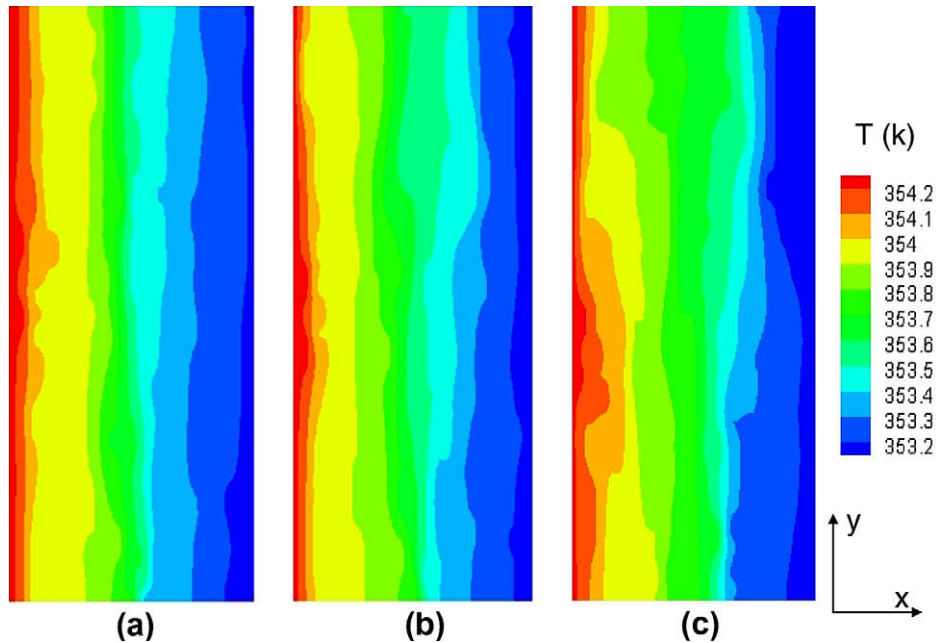

Fig. 8. Temperature contours at different portions of the GDL for $\alpha = 0.05$: (a) $\bar{z} = 0.25$; (b) $\bar{z} = 0.5$; and (c) $\bar{z} = 0.75$. $\bar{z}$ is the dimensionless distance in z direction.

length through the pores to the shortest distance between two points, which lowers in combination with the porosity the effective mass transport in the medium

$$D_g^{k,eff} = \frac{\varepsilon}{\tau} D_g^k \tag{23}$$

The above formula was suggested from the straight-capillary-tube model [42] and volume averaging [43]. Note that several empirical and analytical relations between the porosity and the tortuosity exist because in contrast to the porosity the tortuosity can not be

measured directly [44]. Another relationship $D_g^{k,eff} = \frac{\varepsilon}{\tau^2} D_g^k$ as indicated from the incline-capillary-tube model [45] is also frequently used [46,47]. Furthermore, it was shown that the tortuosity may be a function of the temperature, the diffusing species and the pressure [40,48]. Besides this, Sharratt and Mann [49] indicated that the tortuosity may depend on the Thiele modulus if reactions take place inside the porous structures (which is not the case here). Therefore, the tortuosity as defined in Eq. (23) is not a unique defined material constant but a parameter which takes into account several effects. For this reason we would like to name the tortuosity defined above
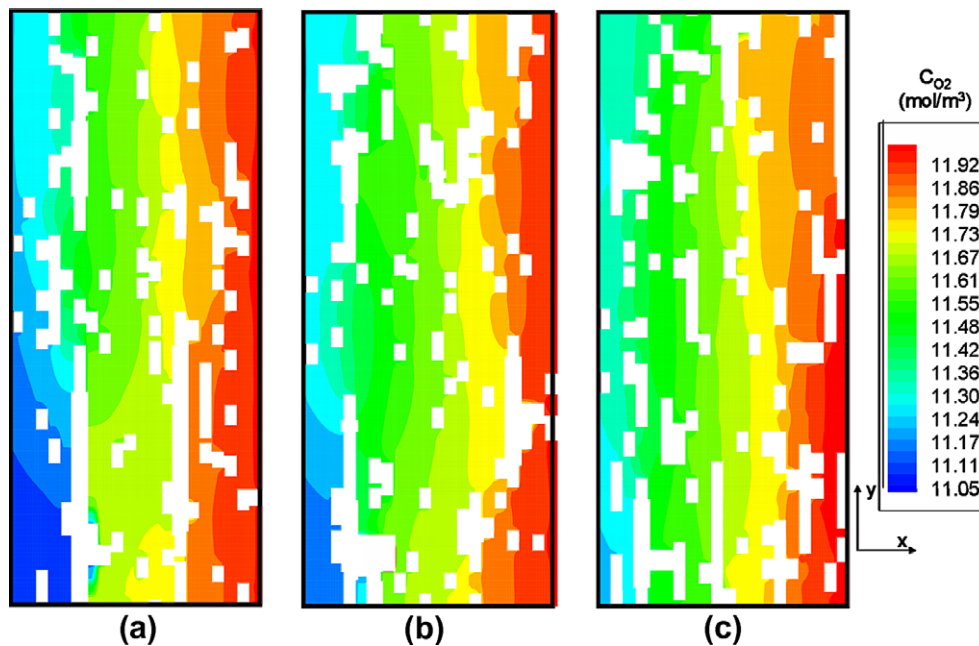
Fig. 9. Oxygen distributions at different portions of the GDL for $\alpha = 0.05$: (a) $\bar{z} = 0.25$; (b) $\bar{z} = 0.5$; and (c) $\bar{z} = 0.75$. $\bar{z}$ is the dimensionless distance in z direction.

as a "transport-based" tortuosity which takes into account the dynamics of the gas transport. In contrast to this in Ref. [36] tortuosity is introduced as a (uniquely defined) local material characteristic which was calculated based on the stochastic model of the GDL. It is also worthy to note that the "transport-based" tortuosity is of significance when dealing with transport phenomena in the GDL.

Due to the anisotropic GDL material the tortuosity differs in through-plane and the in-plane directions. We will focus here on the through-plane one. The "transport-based" through-plane tortuosity as calculated with the direct simulation results in an average value of $\tau = 1.2$. (Notice, that only a small cutout with a small amount of binder was considered.) This is in good agreement with the calculations presented in Ref. [53]. They also examined Toray material but used a slightly different model for the material. They simulated the mass transport using the Lattice–Boltzmann technique. In order to determine the tortuosity they computed the flow path length and averaged over the actual lengths of the flow lines and the flow lines weighted by flux, respectively. Both methods resulted in values which are very close to each other, the flux weighted tortuosity slightly lower. As can be seen in Fig. 11 of Ref. [53] the calculated tortuosity is about $\tau = 1.19$.

Considering the tortuosity as defined in [36] and calculating its value from geometric arguments as was done in Ref. [36] results in slightly higher values. The tortuosities were calculated in three different ways. In the first case the tortuosity was calculated as the shortest pathways from one side to the other side which results in a mean value of $\tau = 1.73$. In the other two cases these pathways were weighted with the capacity ($\tau = 1.71$) and the area ($\tau = 1.73$), respectively.

Only for comparison the well-known Bruggemann equation would result in $\tau = 1.13$ but this relation is unsuitable for describing this kind of porous structure (see e.g. [41]). Overall it can be said, that all calculated tortuosities are in the same order of magnitude, the tortuosities calculated from pure geometric arguments show the highest values. The reason for the deviations is due to the different calculation procedures. The direct simulation (and the Lattice–Boltzmann simulation) calculate the tortuosity with the help of mass transport processes in the fibrous structure and are therefore directly linked to the standard definition of the tortuosity

but the information about the structure of the material under observation is limited.

If calculating the tortuosity from pure geometric arguments using the weighted graph of the pore structure, one gets information about the structure of the material (e.g. tortuosity distribution) but the results are not directly linked to mass transport. In order to link the two tortuosities together further examinations are necessary which are beyond the scope of this paper.

In addition, several studies report utilizing electrical properties in the study of flow through porous media [50,51]. The MacMullin number is defined to measure the ratio of resistance of the porous media saturated with an electrolyte to the bulk resistance of the same electrolyte [50,51], i.e. $\frac{D_g^k}{D_g^{k,eff}}$ for a specific species. This ratio was also called the formation resistivity factor in an earlier work by Archie [52]. In Eq. (23), the MacMullin number is implicitly defined as $\frac{\tau}{\varepsilon}$, and its value from the direct simulation is ~1.6 for the carbon paper considered.

Fig. 10 shows the oxygen and temperature profiles at the cross line of the mid-planes in z and x directions for both $\alpha = 0.05$ and 0.5. These two cases indicate similar flow distribution but with quite different magnitudes. For the oxygen, the concentration along this line shows a small variation in each case, which is attributed to the diffusion that dominates the mass transport. The random solid matrix either leads to blockage of the diffusion or varies local flow, leading to fluctuation of oxygen concentration from place to place. The case of the higher α shows a lower oxygen profile. This can be explained by the fact that a higher α induces a stronger flow towards the gas channel (see Figs. 6(b) and 7(a)). Note that the convection by the flow is against the direction of oxygen diffusion for the reaction. Again the difference is small (~0.1 mol/m^3) due to the relatively weak convection force. Fig. 10(b) presents the temperature profiles, showing the two are very close with the case of $\alpha = 0.5$ slightly lower. This is due to the fact that the flow from the electrode delivers thermal energy therefore helps heat removal, however the amount is small and most is still removed by the highly conductive carbon fiber. Temperature variation near the solid–gas interface is moderate, indicating little heat is transferred between two phases partly
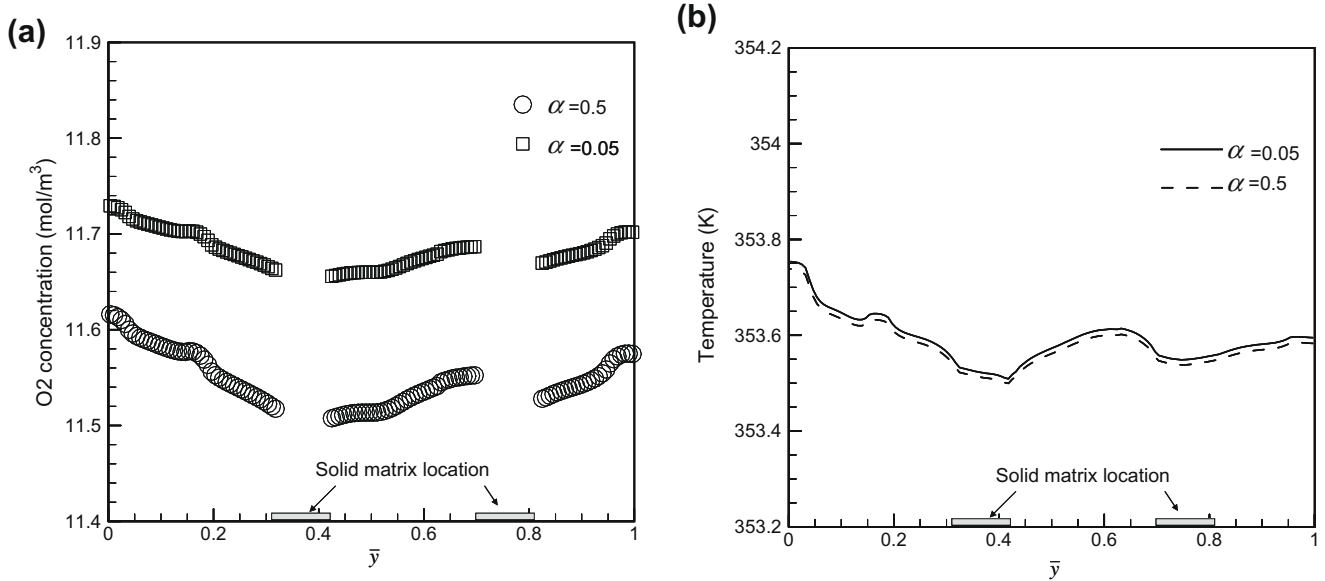
Fig. 10. Distributions of quantities at the cross line of the planes $\bar{z} = 0.5$ and $\bar{x} = 0.5$: (a) the oxygen concentration and (b) temperature. $\bar{z}$ and $\bar{x}$ are the dimensionless distances in z and x directions, respectively.
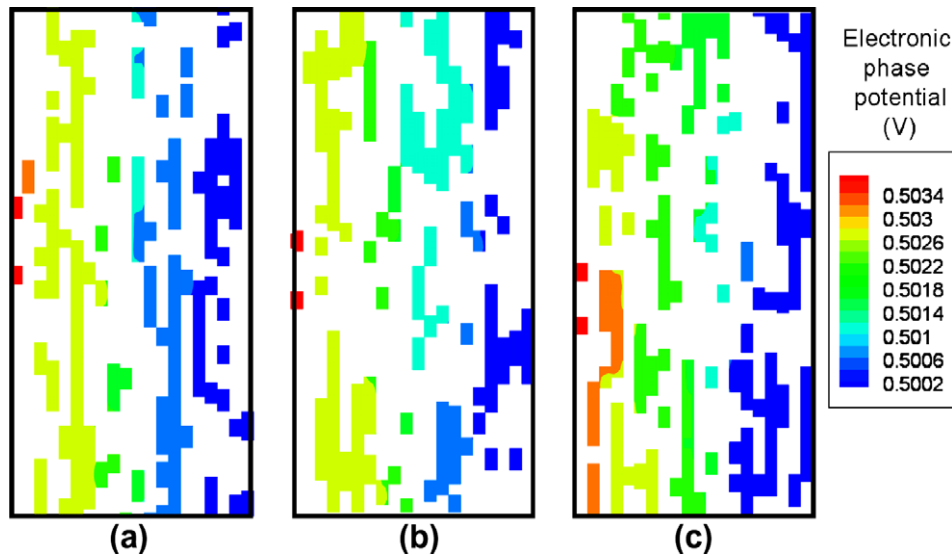

Fig. 11. Electronic phase potential distributions at different portions of the GDL for $\alpha = 0.05$: (a) $\bar{z} = 0.25$; (b) $\bar{z} = 0.5$; and (c) $\bar{z} = 0.75$, where $\bar{z}$ is the dimensionless distance in z direction ranging from 0 to 1.

due to the small gas heat capacity. However, the gas temperature is largely affected by the neighboring carbon fiber due to the small scale of the pore.

Fig. 11 displays the electronic phase potential distributions in the solid matrix at the three locations. Though the figure shows disconnected solid matrix, the fibers are connected in the 3D structure. A small but discernible drop of the electronic phase potential can be observed from the electrode side to the channel. This is because though the carbon fiber is a good thermal conductor, the highly tortuous nature of the solid matrix leads to non-negligible ohmic resistance. Similar to oxygen transport in the pore, electron transport totally relies on the highly tortuous solid matrix. The high tortuosity arises from the fact that the fibers are arranged in the in-plane direction and the through-plane conduction only occurs at the joint points of fibers. By applying a similar approach as Eq. (23) $\left(\sigma_s^{eff} = \frac{(1-\varepsilon)}{\tau_s} \sigma_s \right)$, the tortuosity τ_s is 13.8 for the solid ma-

trix. Again from previous discussion, this tortuosity is referred to the "transport-based" one and may slightly deviate from the material intrinsic property. Further, the obtained tortuosity is for the through-plane transport, which may be different with the in-plane one as the carbon paper is anisotropic. Ref. [6] indicates that the through-plane conductivity is an-order-of-magnitude lower than the in-plane one. This figure shows that the unique structure of the carbon paper, the high through-plane tortuosity, may be a major reason for the relatively lower conductivity in the through-plane direction.

5. Conclusions

This paper combined the stochastic modeling for reconstruction of microstructure of GDLs and direct simulation for study of the mass transport at the pore level. A stochastic model was applied

for the carbon-paper-based GDL, which models the GDL as a stack of thin sections with each section described by planar two-dimensional random line tessellations extended to three dimensions by dilation. The direct simulation was then introduced to the reconstructed GDL structure to simulate the flow and species transport in the void, electronic current conduction in the solid matrix, and heat transfer in both phases. Standard conditions of fuel cells are considered in the simulation. Distributions of the flow, species concentration, temperature, and electronic phase potential in the GDL are presented at the pore level. Simulation results indicated that the through-plane tortuosity of the solid matrix is an-order-of-magnitude larger than the one of the pore structure. The predicted values of tortuosity and permeability are in good agreement with the ones in the literature. In addition, diffusion dominates the species transport in the pore even at high values of net water transfer coefficient. The developed numerical tools can be applied to investigate the pore-level phenomena within the carbon-paper-based GDL. Future study includes investigation of the different realizations of porous materials which allows a statistical analysis of the numerical simulation results and the influence of the compression over the GDL on in-plane and through-plane mass transport.

Acknowledgements

References

[1] M.L. Perry, T.F. Fuller, Conjugated and Fullerene-Containing Polymers for Electronic and Photonic Applications: Advanced Syntheses and Microlithographic Fabrications, J. Electrochem. Soc. 149 (2002) S59–S67.

[2] J. Larminie, A. Dicks, Fuel Cell Systems Explained, second ed., John Wiley & Sons, 2003.

[3] C.Y. Wang, Fundamental models for fuel cell engineering, Chem. Rev. 104 (2004) 4727–4765.

[4] P. Costamagna, S. Srinivasan, Quantum jumps in the PEMFC science and technology from the 1960s to the year 2000: Part I. Fundamental scientific aspects, J. Power Sources 102 (2001) 242–252.

[5] P. Costamagna, S. Srinivasan, Quantum jumps in the PEMFC science and technology from the 1960s to the year 2000: Part II. Engineering, technology development and application aspects, J. Power Sources 102 (2001) 253–269.

[6] M. Mathias, J. Roth, J. Fleming, W. Lehnert, Diffusion Media Materials and Characterization, in: W. Vielstich, H. Gasteiger, A. Lamm (Eds.), Handbook of Fuel Cells: Fundamentals Technology and Applications, vol. 3, John Wiley & Sons, 2003.

[7] C.H. Hartnig, L. Jörissen, J. Kerres, W. Lehnert, J. Scholta, Polymer electrolyte membrane fuel cells (PEMFC), in: M. Gasik (Ed.), Materials for Fuel Cells, Woodhead Publishing Limited, 2008.

[8] J.S. Yi, T.V. Nguyen, Multi-Component Transport in Porous Electrodes in Proton Exchange Membrane Fuel Cells Using the Interdigitated Gas Distributors, J. Electrochem. Soc. 146 (1999) 38.

[9] Y. Wang, C.Y. Wang, Simulations of Flow and Transport Phenomena in a Polymer Electrolyte Fuel Cell under Low-Humidity Operations, J. Power Sources 147 (2005) 148.

[10] S. Dutta, S. Shimpalee, J.W. Van Zee, Three-dimensional numerical simulation of straight channel PEM fuel cells, J. Appl. Electrochem. 30 (2000) 135.

[11] Y. Wang, C.Y. Wang, Modeling Polymer Electrolyte Fuel Cells with Large Density and Velocity Changes, J. Electrochem. Soc. 152 (2) (2005) A445.

[12] S. Mazumder, J.V. Cole, Rigorous 3-D mathematical modeling of PEM fuel cells, J. Electrochem. Soc. 150 (2003) 1503.

[13] J.J. Hwang, Thermal-electrochemical modelling porous electrodes of a PEM fuel cell, J. Electrochem. Soc. 153 (2006) A216.

[14] Y. Wang, C.Y. Wang, A Non-Isothermal, Two-Phase Model for Polymer Electrolyte Fuel Cells, J. Electrochem. Soc. 153 (2006) A1193.

[15] E. Birgersson, M. Noponen, M. Vynnycky, Analysis of a Two-Phase Non-Isothermal Model for a PEFC, J. Electrochem. 152 (2005) A1021.

[16] U. Pasaogullari, C.Y. Wang, Two-phase transport and the role of microporous layer in Polymer Electrolyte Fuel Cells, J. Electrochem. Soc. 151 (2004) A399.

[17] J.-H. Nam, M. Kaviany, Effective diffusivity and water-saturation distribution in single- and two-layer PEMFC diffusion medium, Int. J. Heat Mass Transfer 46 (2003) 4595.

[18] Y. Wang, Modeling of two-phase transport in the diffusion media of polymer electrolyte fuel cells, J. Power Sources 185 (2008) 261–271.

[19] D.M. Bernardi, M.W. Verbrugge, A Mathematical Model of the Solid-Polymer-Electrolyte Fuel Cell, J. Electrochem. Soc. 139 (1992) 2477.

[20] H. Meng, C.Y. Wang, Electron transport in PEFCs, J. Electrochem. Soc. 151 (2004) A358.

[21] H. Meng, A three-dimensional PEM fuel cell model with consistent treatment of water transport in MEA, J. Power Sources 162 (2006) 426.

[22] Y. Wang, Analysis of the Key Parameters in the Cold Start of Polymer Electrolyte Fuel Cells, J. Electrochem. Soc. 154 (2007) B1041–B1048.

[23] P.P. Mukherjee, C.Y. Wang, Stochastic Microstructure Reconstruction and Direct Numerical Simulation of the PEFC Catalyst Layer, J. Electrochem. Soc. 153 (2006) A840.

[24] M. Piller, G. Schena, M. Nolich, S. Favretto, F. Radaelli, E. Rossi, Analysis of Hydraulic Permeability in Porous Media: From High Resolution X-ray Tomography to Direct Numerical Simulation, Transp. Porous Media 80 (2009) 57.

[25] V.P. Schulz, P.P. Mukherjee, J. Becker, A. Wiegmann, C.Y. Wang, Numerical Evaluation of Effective Gas Diffusivity - Saturation Dependence of Uncompressed and Compressed Gas Diffusion Media in PEFCs, ECS Trans. 3 (2006) 1069.

[26] M. Kaviaty, Principles of Heat Transfer in Porous Media, second ed., Springer, 1999.

[27] M. Kaviany, Principles of Convective Heat Transfer, second ed., Springer, 2001.

[28] R. Thiedmann, F. Fleischer, Ch. Hartnig, W. Lehnert, V. Schmidt, Stochastic 3Dmodeling of the GDL structure in PEM fuel cells based on thin section detections, J. Electrochem. Soc. 155 (2008) B391–B399.

[29] V.P. Schulz, J. Becker, A. Wiegmann, P.P. Mukherjee, C.-Y. Wang, Modeling of Two-phase Behavior in the Gas Diffusion Medium of Polymer Electrolyte Fuel Cells via Full Morphology Approach, J. Electrochem. Soc. 154 (4) (2007) B419–B426.

[30] G. Inoue, Y. Matsukuma, M. Minemoto, in: Proceedings of the Second European Fuel Cell Technology and Applications Conference, EFC2007-39024, 2007.

[31] M. Yoneda, M. Takimoto, S. Koshizuka, ECS Trans. 11 (2007) 629–635.

[32] G. Inoue, T. Yoshimoto, Y. Matsukuma, M. Minemoto, Development of simulated gas diffusion layer of polymer electrolyte fuel cells and evaluation of its structure, J. Power Sources 175 (2008) 145–158.

[33] J.T. Gostick, M.W. Fowler, M.A. Ioannidis, M.D. Pritzker, Y.M. Volfkovich, A. Sakars, Capillary pressure and hydrophilic porosity in gas diffusion layers for polymer electrolyte fuel cells, J. Power Sources 156 (2006) 375–387.

[34] R. Schneider, W. Weil, Stochastic and Integral Geometry, Springer, Berlin, 2008.

[35] D. Stoyan, W.S. Kendall, J. Mecke, Stochastic Geometry and its Applications, second ed., John Wiley & Sons, Chichester, 1995.

[36] R. Thiedmann, Ch. Hartnig, I. Manke, V. Schmidt, W. Lehnert, J. Electrochem. Soc. 156 (11) (2009) B1339–B1347.

[37] Y. Wang, X. Feng, Analysis of Reaction Rates in the Cathode Electrode of Polymer Electrolyte Fuel Cells Part I: Single-Layer Electrodes, J. Electrochem. Soc. 155 (12) (2008) B1289–B1295.

[38] S.V. Patankar, Numerical Heat Transfer and Fluid Flow, Hemisphere, New York, 1980.

[39] J.P. Feser, A.K. Prasad, S.G. Advani, Experimental characterization of in-plane permeability of gas diffusion layers, J. Power Sources 162 (2006) 1226–1231.

[40] F. Keil, Diffusion und Chemische Reaktionen in der Gas/Feststoff–Katalyse, Springer, Berlin, 1999.

[41] L. Shen, Z. Chen, Critical review of the impact of tortuosity on diffusion, Chem. Eng. Sci. 62 (2007) 3748–3755.

[42] M.R.J. Wyllie, M.B. Spangler, Application of electrical resistivity measurements to problem of fluid flow in porous media, Am. Assoc. Pet. Geol. Bull. 36 (1952) 359.

[43] S. Liu, J.H. Masliyah, in: K. Vafai (Ed.), Handbook of Porous Media, CRC Press, Boca Raton, FL, 2005, pp. 81–140.

[44] Y.S. Wua, L.J. van Vliet, H.W. Frijlink, K. van der Voort Maarschalk, The determination of relative path length as a measure for tortuosity in compacts using image analysis, Eur. J. Pharm. Sci. 28 (2006) 433–440.

[45] D. Cornell, D.L. Katz, Flow of gases through consolidated porous media, Ind. Eng. Chem. 45 (1953) 2145.

[46] K.M. Abraham, Directions in secondary lithium battery research and development, Electrochim. Acta 38 (1993) 1233.

[47] D. Djian, F. Alloin, S. Martinet, H. Lignier, J.Y. Sanchez, Lithium-ion batteries with high charge rate capacity: Influence of the porous separator, J. Power Sources 172 (2007) 416.

[48] S.K. Bhatia, Stochastic theory of transport in inhomogeneous media, Chem. Eng. Sci. 41 (1986) 1311.

[49] P.N. Sharratt, R. Mann, Some observations on the variation of tortuosity with Thiele modulus and pore size distribution, Chem. Eng. Sci. 42 (7) (1987) 1565–1576.

[50] R.B. MacMullin, G.A. Muccini, Characteristics of porous beds and structures, AIChE J. 2 (1956) 393.

[51] M.J. Martinez, S. Shimpalee, J.W. Van Zee, Measurement of MacMullin Numbers for PEMFC Gas-Diffusion Media, J. Electrochem. Soc. 156 (2009) B80.

[52] G.E. Archie, The electrical resistivity log as an aid in determining some reservoir characteristics, Trans. Am. Inst. Min. Metall. Pet. Eng. 146 (1942) 54.

[53] L. Hao, P. Chen, Lattice Boltzmann simulations of anisotropic permeabilities in carbon paper gas diffusion layers, J. Power Sources 186 (2009) 104–114.